DOI: 10.1111/cgf.14893
Eurographics Symposium on Rendering 2023
T. Ritschel and A. Weidlich
(Guest Editors)

COMPUTER GRAPHICS *forum*
Volume 42 (2023), Number 4
e14893 *pp. 1 - 15*

Iridescent Water Droplets Beyond Mie Scattering

Mengqi (Mandy) Xia[1,2] Bruce Walter[1] Steve Marschner[1]

[1]Cornell University [2]EPFL

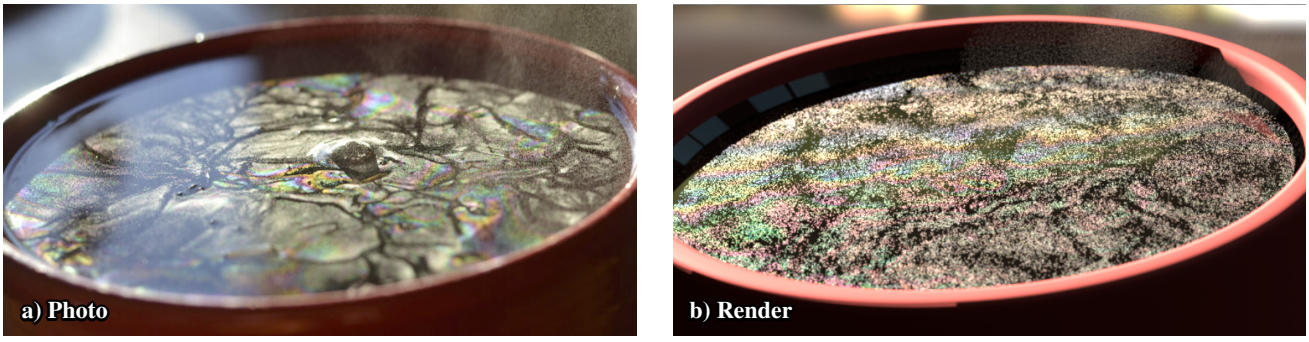

Figure 1: *Hot tea lit by sunlight (a) forms a layer of levitating droplets that appear colored due to interference between scattered and reflected paths, a phenomenon known as Quetelet scattering. To render this scene (b), we use our new scattering model to render a collection of droplets, with density according to an image texture and parameters inferred from thermal imaging of a hot water surface. We also render steam particles above the water surface. This paper analyzes the causes of iridescence in levitating droplets and steam and shows how to render both phenomena. Photo by Vivien Parmentier.*

Abstract

Looking at a cup of hot tea, an observer can see color patterns and granular textures both on the water surface and in the steam. Motivated by this example, we model the appearance of iridescent water droplets. Mie scattering describes the scattering of light waves by individual spherical particles and is the building block for both effects, but we show that other mechanisms must also be considered in order to faithfully reproduce the appearance. Iridescence on the water surface is caused by droplets levitating above the surface, and interference between light scattered by drops and reflected by the water surface, known as Quetelet scattering, is essential to producing the color. We propose a model, new to computer graphics, for rendering this phenomenon, which we validate against photographs. For iridescent steam, we show that variation in droplet size is essential to the characteristic color patterns. We build a droplet growth model and apply it as a post-processing step to an existing computer graphics fluid simulation to compute collections of particles for rendering. We significantly accelerate the rendering of sparse particles with motion blur by intersecting rays with particle trajectories, blending contributions along viewing rays. Our model reproduces the distinctive color patterns correlated with the steam flow. For both effects, we instantiate individual droplets and render them explicitly, since the granularity of droplets is readily observed in reality, and demonstrate that Mie scattering alone cannot reproduce the visual appearance.

CCS Concepts

• ***Computing methodologies*** → ***Reflectance modeling; Ray tracing;***

1. Introduction

Water often forms small particles that interact with light in beautiful and surprising ways, and in this paper we focus on very small droplets in small-scale scenes. Our motivating example (seen in the accompanying video) is a cup of hot tea, where the right lighting conditions reveal color patterns dancing across the water surface and in the steam rising from the cup.

In this paper, we explain these two appearance effects, each an instance of a broader phenomenon, and build models that combine aspects of dynamics and appearance to reproduce them. Specifi-

© 2023 Eurographics - The European Association
for Computer Graphics and John Wiley & Sons Ltd.

delivered by EUROGRAPHICS DIGITAL LIBRARY www.eg.org diglib.eg.org

cally, iridescence on the water surface is an example of Quetelet scattering, an optical interference pattern occurring at a reflective surface covered by particles; and iridescence in steam is driven by the dynamics of condensation and evaporation, which changes droplet sizes, and therefore scattering properties, over time.

We compare three different Quetelet scattering models with different accuracy and select a first-order model that exactly accounts for single scattering by the particles with reflection from the surface before and/or after scattering. To get the required parameters, we build an empirical model that relates temperature to droplet size and height with the aid of thermal infrared images. Based on this scattering model we implement a Quetelet phase function, to render particle collections on surfaces, and a Quetelet BRDF, to render surfaces when individual granules are not visible. We validate our model against Quetelet patterns photographed on a mirror dusted with monodisperse silica particles.

For steam iridescence, we identify droplet size variation as an essential contributor to the distinctive color patterns in steam. Based on the output of an existing fluid simulator, we introduce a model for the growth and shrinkage of droplets due to condensation and evaporation, which enables us to instantiate individual droplets with realistic size variations. Combining this with Mie scattering, we produce iridescent steam whose color patterns resemble real video of steam much more closely than simply using uniform size droplets. To efficiently render large numbers of fast-moving, sparse steam particles with motion blur, we adopt a technique in motion blur [NSG11], which intersects rays with particle trajectories and blends contributions along viewing rays. This achieves 10x speed up compared to the brute force temporal sampling method.

The familiar model of Mie scattering from wave optics is a building block for both models, but we explain and demonstrate that reproducing the appearance of Quetelet scattering and steam iridescence requires applying Mie scattering in the context of other phenomena, namely interference and droplet dynamics. By adding this context, we extend the range of particle scattering effects that can be rendered in computer graphics and provide the tools to reproduce other appearance phenomena, such as iridescent clouds or dusty specular surfaces, which stem from the same causes. This work shows the value of considering dynamics and appearance together and demonstrates how an integrated study of physics simulation and rendering can improve the rendering of complex materials.

2. Related Work

Before discussing how to model and reproduce iridescent levitating drops and steam, we will review relevant computer graphics literature on topics including physics literature on Quetelet scattering and levitating drops, as well as iridescence and wave optics models for scattering and reflection.

Volume scattering and atmospheric phenomena. Lorenz-Mie theory describes the scattering of an electromagnetic plane wave by a homogeneous sphere and is widely used in atmospheric optics [vdHul57]. In computer graphics, Frisvad et al. [FCJ07] applied Mie scattering, which we also use as one component of our models, to compute the scattering properties of participating media and translucent materials. Guo et al. [GJZ21] relax the far-field scattering assumption and present a framework that considers near-field light transport between particles.

When thinking of colorful water droplets, the first phenomenon that comes to mind is probably the rainbow, with its multicolored arcs appearing when sunlight illuminates falling rain. To render rainbows, Sadeghi et al. [SML*12] propose a wavefront tracing algorithm, since Mie scattering is not suitable in their case because raindrops are too large to be modeled accurately as spheres. In this paper, we explore other types of color effects in water droplets that are quite distinct from the rainbow. Water droplets in steam are on the scale of several to tens of microns as compared to millimeters for raindrops, and the scene scale is much smaller, so the granularity of droplets is visible. The major cause of color in the rainbow is dispersion (variation of refractive index with wavelength), whereas in our problem, colors are produced by interference and diffraction, and dispersion is not necessary to simulate them.

Regarding atmospheric phenomena, there are also many methods for rendering the sky [BN08; NSTN93; Wen07; HW12]. These works all render continuous volumes using radiative transfer, while we instantiate particles and render them directly.

Levitating droplets and Quetelet scattering. Droplets levitating above a hot water surface are a fascinating phenomenon that has been actively studied in the physics community [Fed04; Fed05; FDN17; UONI15]. The most widely accepted explanation is that the Stokes drag force in the rising evaporation flow [Fed05] holds droplets away from the surface. The levitation height depends on the local air flow, which is influenced by the surface temperature. Researchers are trying to better explain and model the mechanism of levitation, as well as verify the relationship between levitation height, radius, and temperature. Water droplets also tend to form regular clusters [Fed12] above the water surface. Related levitating phenomena can also be found over a solid surface [ZKAK17]. Ajaev et al. [AK21] provide a recent survey of this topic.

We identify that the interference between light paths scattered by the drops and reflected by the water surface is essential to the color patterns we observe. This effect is known as Quetelet scattering, named after the astronomer Adolphe Quetelet, who studied it. Bobbert et al. [BVG86] modeled it using Debye potentials, while Wriedt et al. [WD98] derived an equivalent formulation using spherical wave functions that is more compact and amenable to numerical evaluation [Mac08]. Germer [Ger97] introduced a model that accounts for the interference between all first-order paths, considering only far-field interactions between the sphere and the surface and assuming the observer is far away. Further approximations can be made by introducing a virtual sphere below the water surface using mirror-image symmetry. This is called the bi-sphere model and was proposed by Suhr et al. [SS09]. In our work, we compare these three models and show that the first-order model is suitable for our application as it is efficient and has good accuracy when not close to the normal direction. Note that Quetelet scattering is different from thin-film iridescence [BB17] and, since spheres scatter differently than surfaces, the color predictions are different. Previously in rendering, Gu et al. [GRBN07] modeled and rendered dusty windows using radiative transport theory, but they did not consider Quetelet scattering or other wave optics effects in their

© 2023 Eurographics - The European Association for Computer Graphics and John Wiley & Sons Ltd.

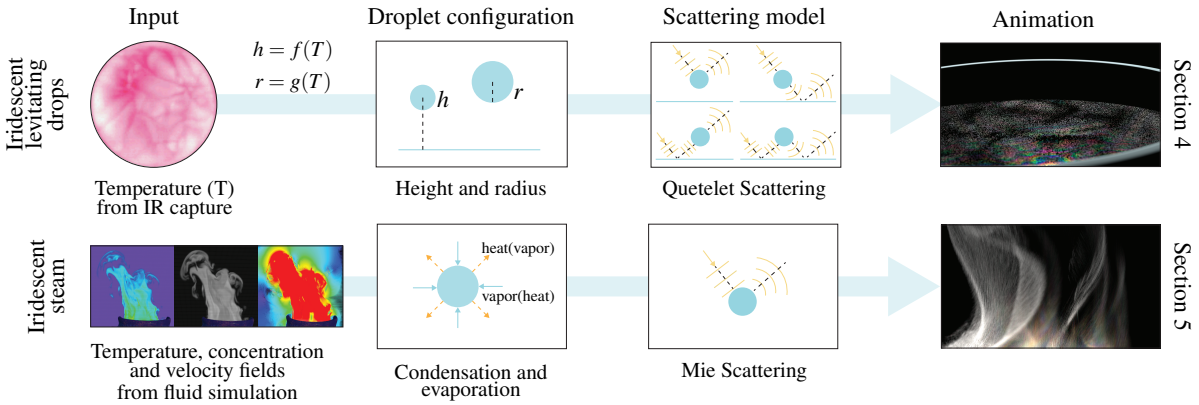

Figure 2: *An overview of generating and rendering iridescent levitating droplets and steam. For levitating drops, we capture temperature information using an infrared camera and predict the height and radius of the drops using an empirical model (Section 4.2). These parameters are used in a Quetelet scattering model to compute interference between light scattered by particles and reflected by the surface (Section 4.1). This produces color patterns on the water surface. For steam, we use our droplet growth model to post-process temperature, concentration and velocity fields from an existing fluid simulation to drive droplets' motion and size variation based on their histories. Then we render droplets explicitly using Mie scattering to reproduce color patterns in the steam.*

model. Quetelet scattering phenomena are readily observable but have not previously been modeled and reproduced in rendering.

Steam in computer graphics has been simulated similarly to smoke using fluid simulation [Sta99b; FSJ01; ZBG15]. Steam is often rendered using radiative transfer as a continuous volume, and usually particles are not instantiated. However, as we can see in the capture, the discreteness of water droplets is visible when we are close to the steam. In our work, we make use of an existing fluid simulation (the Pyro solver in Houdini 18.5) and adopt a diffusive droplet growth model [PK12] to model the condensation and evaporation of droplets. This allows us to acquire droplet sizes for each frame. With precise droplet geometry and position, we are able to render collections of drops explicitly using Mie scattering. Color effects in steam have been observed and recorded [Ste09], but they have not been previously modeled or rendered. To efficiently render droplets in the steam with motion blur, we use a capsule primitive that extends a sphere into a swept volume. Tracing the swept volume is a technique that has been used for rendering motion blur [NSG11; Van85; Lei95; SYK*17]. A similar idea has been applied to anisotropic surface roughness and to account for the temporal surface normal variation due to motion blur [THDD20].

Granular media. Media consisting of visible particles has been studied in rendering. Moon et al. [MWM07] precomputed shell transport functions that summarize the spatio-angular light transport within assemblies of discrete particles. Müller et al. [MPG*16] rendered heterogeneous and dynamic granular mixtures with spatially varying grain properties. Zhang et al. [ZZ20] proposed a symbolic and differentiable Monte Carlo process to render grains with different properties that can reuse a single precomputation. Guo et al. [GHC*22] applied a geometrical optics approximation (GOA) to render discrete media with different particle distributions. Unlike these works, we render fast-moving assemblies and explicitly represent individual droplets.

Wave optics based scattering models and light transport. In addition to using Mie scattering to render participating media, wave optics have also been extensively used for modeling rough surface reflectance. For instance, models have been developed for surfaces with random [HTSG91] or periodic [Sta99a; HP17] stationary statistics, and for predicting the average [DWMG16] and fine-scale appearance [YHW*18] of surfaces with known geometric microstructures or fine scratches [WVJH17]. Recently, Xia et al. [XWM*20] developed a wave optics fiber scattering model based on full wave simulation. Guillén et al. [GMG*20] developed a material model for pearlescent materials. Beyond wave-based scattering models, researchers have also applied wave optics to the light transport problem [SSY22; SY21]. In our work, we focus on the material level, specifically the wave optics effects produced by spherical particles and specular surfaces.

3. Overview

Colors on hot water surfaces and in steam are both caused by light scattering from droplets, and the sizes and positions of these droplets are dictated by their environment. In this section, we summarize the mechanisms behind these phenomena and our pipelines to reproduce each appearance effect.

In both effects, the droplet size is on the scale of microns, so due to surface tension, the droplets can be approximated as spheres. Mie scattering is therefore very useful in modeling these optical phenomena—but it alone is not enough to reproduce the effects.

3.1. Iridescent levitating droplets

In Figure 1 and the supplemental video, we can observe granular dots on the water surface. These are levitating droplets, and the strong colors that sometimes arise are due to Quetelet scattering

© 2023 Eurographics - The European Association for Computer Graphics and John Wiley & Sons Ltd.

(see Section 2). We propose a scattering model for spherical particles near a surface, which takes the particle size and particle-to-surface distance as input and predicts the rings, stripes, and colors observed in a range of conditions. Based on this model, we propose both a Quetelet scattering phase function, used for rendering individual particles in scenes where they are visible (Figures 1, 12), and a Quetelet scattering BRDF, used to render surfaces when individual granules are not visible (Figures 3, 6, 8, 9).

To model the temporally and spatially varying parameters of our Quetelet scattering model, we propose an approximate empirical model, calibrated by observations of cooling water surfaces, that relates surface temperature with droplet height and size. The overall pipeline for reproducing colors in levitating droplets, illustrated in Figure 2 top, involves first acquiring temperature fields using an infrared camera, then predicting spatially varying droplet height and size, and finally using our Quetelet scattering model in a ray tracer to render the appearance.

Figure 3: *Besides the levitating water drops, Quetelet scattering can be also observed on other surfaces. This is a photograph[Boy09] of a window covered by dust particles and lit by sunlight exhibits Quetelet stripes.*

3.2. Iridescent steam

Steam is produced when water vapor rises from hot water and condenses on pre-existing nuclei in the air. Mie theory accurately models scattering from spherical droplets. However, Mie scattering with uniform-sized particles predicts stable concentric arcs of color around the light source. The main visual feature of steam iridescence is the fleeting color patterns observed mostly near the edges of plumes of steam. This is because condensation and evaporation, which depend on local temperature and humidity, produce rapid changes in droplet size. Modeling this size variation is essential to the appearance. To faithfully reproduce this effect, we first simulate fluid flow, then model droplet growth, and finally ray trace the droplets in the pipeline illustrated in Figure 2 bottom. Rendering these large collections of sparse, fast-moving particles is very slow with conventional temporal sampling. We propose to approximate the mean of a random temporal sampling process by intersecting rays against particle trajectories, rather than against particle positions at particular times. We assume that the probability of hitting a particle, conditioned on having intersected its trajectory, is independent of other particles along the ray. This leads to a simple alpha blending computation for the final color of the ray.

In Sections 4 and 5, we will further discuss Quetelet scattering and iridescent steam models. In Section 6, we provide practical details about rendering, including the motion blur algorithm. We present results in Section 7, and discuss limitations and further applications in Section 8.

4. Quetelet scattering and iridescent levitating droplets

Quetelet scattering (or Quetelet rings) is an interference phenomenon caused by fine particles that are at a consistent distance from a reflective surface. As shown in Figure 3, this can be readily observed on a flat, smooth surface coated with dust or dirt, such as an exterior window or dusty bathroom mirror, appearing as stripes near the reflected image of a strong light source. We will first describe several models that we could use to simulate Quetelet scattering, explain why we chose one specific model for our application, and then discuss how we acquire the parameters for this model.

4.1. Quetelet scattering

The color in Quetelet scattering is mainly caused by interference between different light paths that involve scattering from spheres and reflection from the specular surface underneath. Figure 4 illustrates the first-order light paths that contribute to this phenomenon, where order refers to the number of interactions between the light and the particle. There are in theory infinitely many scattering orders to be considered, and the most accurate way to compute scattering from this system is to fully account for the near-field interaction between the sphere and the specular surface. In the following, we will first describe the exact model, then explain how to apply a first-order approximation to significantly improve the efficiency without losing much accuracy. We will also briefly mention a bi-sphere model used to simulate Quetelet scattering and show that this further approximation results in noticeable visual differences in all cases. Thus in practice we use the first-order model to simulate Quetelet scattering. When we discuss the wave optics models used for Quetelet scattering, we assume time-harmonic waves so we can drop the time dependence and operate only on complex-valued phasors.

4.1.1. Exact solution

Bobbert et al. [BV86; BVG86] developed an exact solution to the sphere-on-surface scattering problem that in theory can account for all orders of near-field interaction between the sphere and the surface. The method applies Debye potentials to expand both the incident wave and the scattered wave into the same set of basis functions, then relates the coefficients using a linear system. Following their notation, we use $\mathbf{V}^{\mathrm{i}}$ to denote (the coefficients of) the directly incident plane wave, $\mathbf{V}^{\mathrm{ir}}$ to denote the incident wave that is reflected by the surface, $\mathbf{W}^{\mathrm{s}}$ to denote the wave that is scattered by the sphere, and $\mathbf{V}^{\mathrm{sr}}$ to denote the scattered wave from the sphere reflected by the surface. Scattering and reflection are linear operations on wave fields that can be expressed as linear transformations

© 2023 Eurographics - The European Association for Computer Graphics and John Wiley & Sons Ltd.

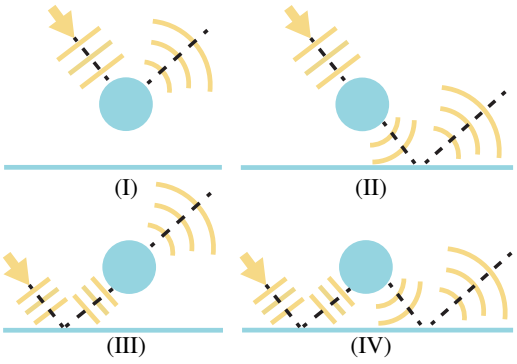

Figure 4: *The first-order paths in Quetelet scattering are those that scatter from the sphere exactly once. There are four types: (I) Light only scattered by the sphere—this is simply Mie scattering. (II) Light first scattered by the sphere and then reflected by the water surface. (III) Light first reflected by the water surface and then scattered by the sphere. (IV) Light reflected by the water surface twice, scattering once in between.*

of the coefficient vectors, and we let the matrix $\mathbf{A}$ characterize reflection from the surface while matrix $\mathbf{B}$ characterizes scattering from the spherical particle. We write out the relations

$$\mathbf{W}^{\mathrm{s}} = \mathbf{B}\left(\mathbf{V}^{\mathrm{i}} + \mathbf{V}^{\mathrm{ir}} + \mathbf{V}^{\mathrm{sr}}\right), \quad \mathbf{V}^{\mathrm{sr}} = \mathbf{A}\mathbf{W}^{\mathrm{s}}. \tag{1}$$

Then $\mathbf{W}^{\mathrm{s}}$ can be solved in terms of $\mathbf{V}^{\mathrm{i}}$ and $\mathbf{V}^{\mathrm{ir}}$:

$$\mathbf{W}^{\mathrm{s}} = (\mathbf{1} - \mathbf{B}\mathbf{A})^{-1}\mathbf{B}\left(\mathbf{V}^{\mathrm{i}} + \mathbf{V}^{\mathrm{ir}}\right). \tag{2}$$

For more details, we refer the reader to the original papers [BV86; BVG86]. In practice, the exact solution is expensive to compute for the particle sizes we are interested in because it involves inverting a matrix $(\mathbf{1} - \mathbf{B}\mathbf{A})$, whose size increases with the particle size. Additionally, every scattering function evaluation requires a matrix-vector multiplication (Equation (2)). An approximate model is more suitable in the rendering context and will be discussed in the following.

4.1.2. First-order model

Germer [Ger97] introduced a model that accounts for the interference between all first-order paths, considering only far-field interactions between the sphere and the surface and assuming that the observer is far away. When only considering the first-order paths, the total contribution is the sum of the four path types shown in Figure 4.

These effects are polarization-dependent, so we need to keep track of the light's polarization throughout these events. This is done using Jones vectors and matrices. The light is represented as a sum of two polarizations, represented as a 2-vector, and each interaction is represented by a 2x2 scattering matrix $\mathbf{S}$ (also called an S-matrix) that transforms from the incident polarization components to the outgoing ones. Different events may be most easily expressed using different choices for the polarization basis, so 2x2 rotation matrices $\mathbf{R}$ are used to transform between different representations of polarization.

To compute the total contribution, we first define the polarization coordinates for incoming and outgoing waves. We then establish the relation between the incident wave and the outgoing wave by relating the two polarization components in each coordinate for each path type. Finally, we sum the four path types together coherently.

Figure 5 shows the polarization frames for the incoming and outgoing waves. We use p and s to represent parallel and perpendicular polarizations respectively. The perpendicular polarization direction, the parallel polarization direction and the wave propagation direction form a right handed frame. The polarization frame for the incoming wave is defined by the incoming direction and the surface normal. $\mathbf{e}_p^i$ denotes the direction of the p-polarized field that is normal to the incident direction and in the plane defined by the incoming direction and the surface normal. $\mathbf{e}_s^i$ denotes the direction of the s-polarized field that is normal to the above plane. The incident electric field $\mathbf{E}^i$ can be decomposed as $\mathbf{E}^i = E_p^i\mathbf{e}_p^i + E_s^i\mathbf{e}_s^i$ and can be represented using the two scalar polarization coefficients E_p^i and E_s^i. Similarly the polarization frame of the outgoing (scattered) wave is defined by the outgoing direction and the surface normal. The scattered electric field $\mathbf{E}^s$ can be written as $\mathbf{E}^s = E_p^s\mathbf{e}_p^s + E_s^s\mathbf{e}_s^s$, where E_p^s and E_s^s are the corresponding polarization coefficients. The incident and the scattered fields in the far-field region can be related using the scattering (Jones) matrix $\mathbf{S}$

$$\begin{pmatrix} E_p^{\mathrm{s}} \\ E_s^{\mathrm{s}} \end{pmatrix} = \frac{e^{-jkL+j\mathbf{k}\cdot\mathbf{L}}}{jkL}\mathbf{S}\begin{pmatrix} E_p^{\mathrm{i}} \\ E_s^{\mathrm{i}} \end{pmatrix} \tag{3}$$

$$= \frac{e^{-jkL+j\mathbf{k}\cdot\mathbf{L}}}{jkL}\begin{pmatrix} S_{pp} & S_{ps} \\ S_{sp} & S_{ss} \end{pmatrix}\begin{pmatrix} E_p^i \\ E_s^i \end{pmatrix}. \tag{4}$$

In the above equations, the $2x2$ matrix $\mathbf{S}$ relates the parallel and perpendicular components of the incident wave and the scattered wave. $\mathbf{k}$ is wave vector, k is wave number, $\mathbf{L}$ is the vector pointing from the source to the detector and L is the distance from the scatterer to the detector.

We would like to compute the scattering matrix $\mathbf{S}$ for Quetelet

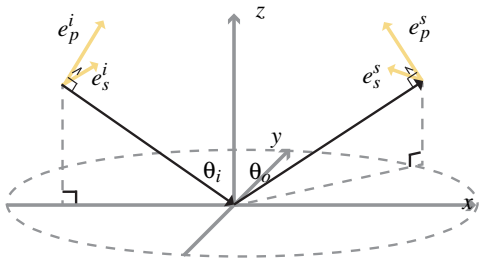

Figure 5: *This figure illustrates the polarization coordinates for the incident wave and the outgoing wave. The incoming wave is decomposed into the parallel (p) polarized direction e_p^i and the perpendicular (s) polarized direction e_s^i. The outgoing wave field is decomposed into the parallel (p) polarized direction e_p^s and the perpendicular (s) polarized direction e_s^s.*

© 2023 Eurographics - The European Association
for Computer Graphics and John Wiley & Sons Ltd.

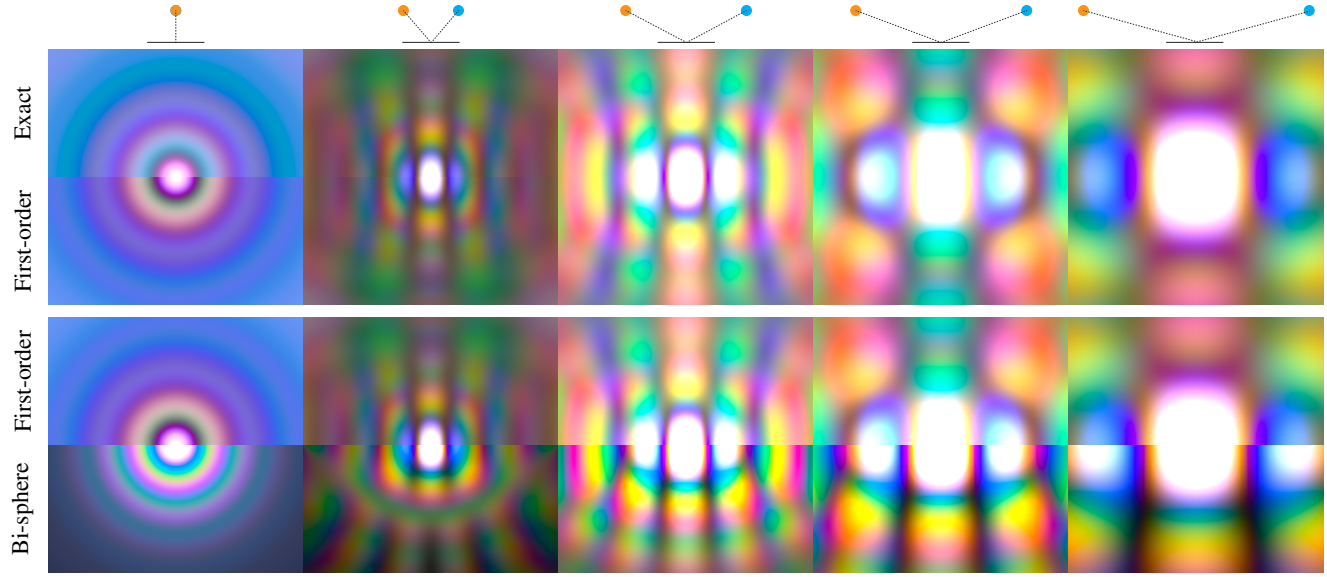

Figure 6: *In the first row, we compare the exact (top half) and the first-order (bottom half) Quetelet scattering models. In the second row, we compare the first-order (top half) and the bi-sphere (bottom half) models. We visualize the full spectrum of the scattering function integrated to RGB color. Each patch is a* 20cm *by* 20cm *surface covered by virtual particles with a radius of* 1μm *and a height of* 2μm*. The point light and the sensor are positioned at a height of 15cm and always above the horizontal center line. Each column corresponds to a different horizontal placement of the light and sensor, with the distance to the center being* $0, 10, 20, 30,$ *and* 40cm *and symmetric around the center. In the first row, we observe that higher-order terms are only important when we are close to the normal direction (first column), and the difference between the exact model and the first-order model becomes invisible as we move away from the normal direction. In the second row, since it lacks the Fresnel factor, the bi-sphere model has large intensity differences with the other two models. Here we rescale it to better match the other models' intensities, but even so, there are still major differences in the scattering functions. From this comparison, we conclude that the first-order model is very similar to the exact model except for near-normal directions (where our droplet iridescence is harder to observe anyway), while the bi-sphere model has large errors at many angles.*

scattering and it can be written as the sum of the scattering matrix of each path type: $\mathbf{S} = \mathbf{S}_{\mathrm{I}} + \mathbf{S}_{\mathrm{II}} + \mathbf{S}_{\mathrm{III}} + \mathbf{S}_{\mathrm{IV}}$. Each component has a Mie scattering contribution as the light is scattered by a sphere once in each path type. We use $\mathbf{S}_{\mathbf{Mie}}$ to denote the Mie scattering matrix of the particle alone. Calculation of $\mathbf{S}_{\mathbf{Mie}}$ can be found in Section 9.31 in [vdHul57]. Mie scattering can be conveniently computed in the polarization coordinates where parallel polarization is within the scattering plane defined by the directions directly incident and existent on the sphere. We use $\mathbf{R}$s to perform rotation between different polarization coordinates. The four scattering matrices corresponding the four path types can be written as

$$\begin{aligned} \mathbf{S_I} &= \mathbf{R_I^{out}} \mathbf{S_{Mie}} \mathbf{R_I^{in}}, \quad \mathbf{S_{II}} = \beta \mathbf{F_s} \mathbf{R_{II}^{out}} \mathbf{S_{Mie}} \mathbf{R_{II}^{in}} \\ \mathbf{S_{III}} &= \alpha \mathbf{R_{III}^{out}} \mathbf{S_{Mie}} \mathbf{R_{III}^{in}} \mathbf{F_i}, \quad \mathbf{S_{IV}} = \alpha\beta \mathbf{F_s} \mathbf{R_{IV}^{out}} \mathbf{S_{Mie}} \mathbf{R_{IV}^{in}} \mathbf{F_i}. \end{aligned} \tag{5}$$

In the above equations, $\alpha = e^{2jkh\cos\theta_i}$ and $\beta = e^{2jkh\cos\theta_s}$ are the phase associated with the path-length difference where h is the levitation height (distance from the surface to the center of the particle). $\mathbf{F_i}$ and $\mathbf{F_s}$ are the Fresnel reflection matrices corresponding to the incident direction and scattering direction, and are diagonal matrices where the diagonal entries are the complex amplitude reflection coefficients for parallel and perpendicular polarizations respectively (Appendix A). The average of the square of these factors is the familiar Fresnel factor used in traditional rendering. Note that this method can be applied to arbitrary particle shapes as long as its scattering matrix is available. This model misses higher order paths, but in our comparison test (Figure 6 top) the visual differences between the first-order model and the exact computation can be neglected when the incident direction and outgoing direction are not both very close to the normal direction of the surface. In order to observe the iridescence on water surface we need to be sufficiently far away from the normal direction. Moreover, the evaluation of the first-order model is 50 to 100x faster than the exact model for the particle configuration we are interested in. Therefore we adopt the first-order model in practice.

4.1.3. Bi-sphere model

We can further approximate the model by using mirror-image symmetry and introducing a virtual sphere below the water surface. This is known as the bi-sphere model, which was proposed by Suhr et al. [SS09]. Figure 7 illustrates this idea, where the dashed-line sphere represents the image of the real particle mirrored by the surface. With this symmetry, we can easily compute interference between paths of type II and type III (Figure 4). However, their model is missing the interference between other path combinations, the phase change at reflection, and the Fresnel factor at reflection.

© 2023 Eurographics - The European Association for Computer Graphics and John Wiley & Sons Ltd.

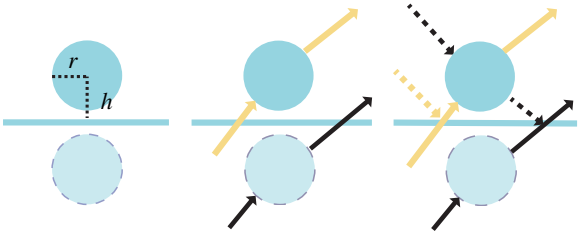

Figure 7: *The bi-sphere model can be considered as introducing an imaginary sphere with reflection symmetry to the original sphere across the water surface (left figure). Adding Mie scattering from the two spheres (middle figure) computes the interference between path type II and type III in the first-order paths (right figure).*

Based on our test (Figure 6 bottom), the interference pattern produced by the bisphere model can be substantially different from the result generated by the first-order model. Therefore, we do not use the bisphere model in our application.

4.2. Droplet configuration

To produce levitating drops, we must determine their levitation height and droplet size. Previous studies of levitating droplets used microscopes to directly measure droplet size and height [UONI15; Fed04; Fed05]. We take a different approach and use thermal and optical images to create an empirical model that relates water surface temperature to droplet size and height.

Our size and height data come from images of a hot water surface, like the one shown in Figure 8 (a). In these images, we observe a bright reflection of the light source surrounded by colorful rings and stripes. We take these images out of focus, since the blur averages over the particles and makes the color pattern more regular. As we see in Figure 8, the size of the colorful rings depends on the average droplet radius (r), and the width of the stripes depends on the average droplet height (h). Therefore, by comparing the renders and the optical images, we can estimate these parameters. We take synchronized thermal and optical images as the water cools, using the thermal images to estimate the average surface temperature T. This produces a set of (T, r, h) triples from which we build an empirical model using linear regression (see the supplementary material for details):

$$\begin{aligned} r &= 0.1613T - 5.5078 \\ h &= 0.2679T - 8.2595, \end{aligned} \tag{6}$$

Where r denotes the radius in microns, h is the distance from the water surface to the droplet center in microns, and T is the temperature in degrees Celsius. Note that the pattern is concentrated in Figure 8 a), while the patterns are consistent throughout the spatial domain for the renders. This is because we use a Quetelet BRDF to render b) - d), and we did not match the density of the particles for this example.

4.3. Validation

It is difficult to conduct repeatable and controllable experiments for levitating drops. Therefore, we used solid spheres on a mirrored surface to create an optically similar setup for validation. We distributed monodisperse amorphous silica microspheres (Cospheric SiO2MS-2.0, diameter 9.2μm $\pm$5%, $n \approx 1.4$) on an 18.5x4.8cm rectangular back-surface mirror measuring 1.127mm in thickness. We then photographed the surface from a distance of 159.5cm using a 100mm lens at $f/20$. Illumination was from a white LED positioned 7.8cm above the camera and 7.5cm closer to the mirror. The mirror was oriented to put the image of the source near the center of the mirror.

This experiment differs from the water surface in that there is a layer of glass between the particles and the main reflecting surface, but Quetelet scattering can be easily generalized to multiple specular surfaces beneath the particles (Appendix B). We made this extension to our Quetelet BRDF (Section 6) for this validation and configured it with two specular surfaces: one glass/air interface and one aluminum surface beneath the spheres.

In Figure 9, we compare the photograph (a) to renderings with the same lighting and viewing conditions. Since the particles are uniform in size, the Mie scattering ring is clear, as shown in both the capture and the renders. The size and color of the Mie rings agree well. Quetelet scattering produces horizontal stripes in this viewing configuration, and renders (b) and (c) show Quetelet stripes that have a very similar width, orientation, and color to the photograph.

The color in rendering (b) is more saturated than in the photo, possibly due to irregularity in particle height or to the partial coherence of the light source. In (c) we introduced 0.01% randomness in distance when computing the phase and this produces less saturated colors and more similar appearance to (a). There is also a vertical highlight in the photo, which we attribute to horizontal streaks on the mirror caused while spreading the particles.

5. Iridescent Steam

The iridescence seen in steam (e.g. Figure 11 a) appears as tinges of color that come and go in irregular shapes as the steam moves, occurring within a few degrees of the location of the dominant light source in the image. These features contrast with the rainbow, which occurs when the light is on the same side as the viewer and appears in concentric arcs that are fixed in image space. Besides the difference in scattering angle, steam iridescence occurs only for very small droplets on the order of microns in radius, whereas the rainbow occurs only for large drops on the order of a millimeter [SML*12]. These differences reveal that steam iridescence is a separate phenomenon; the colors are caused by wavelength-dependent diffraction rather than by refraction and dispersion.

Because the droplet size is small in steam, we can safely assume a spherical shape and apply Mie theory to compute light scattering from the droplets. Figure 10 shows that both scattering angle and droplet size affect the Mie color. Therefore, the color observed in the steam varies with changes in both scattering angle and droplet size. To reproduce the effects of size variation, we need to model how droplets grow and shrink due to condensation and evaporation. In this section, we will explain how we build on top of existing fluid simulation in computer graphics to model the motion and changing size of water droplets.

© 2023 Eurographics - The European Association
for Computer Graphics and John Wiley & Sons Ltd.

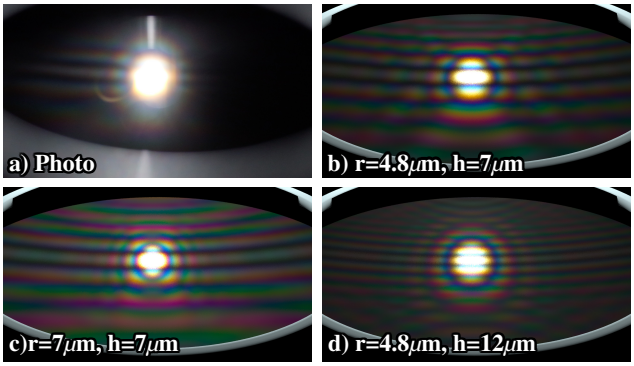

Figure 8: *a) is an out-of-focus capture of the Quetelet stripes on the surface of hot tea (67.7 °C). We observe the bright reflection of the light source, color rings around the reflection, and horizontal color stripes. The Quetelet scattering pattern is clearer in this setting because the out-of-focus blur averages out local variations in the size and height of drops. b) is produced using our model, and its appearance is similar to a) with a radius of 4.8μm and a height of 7μm. In c) and d), we increase the radius to 7μm and the height to 12μm respectively, and observe that larger droplets result in narrower rings, and higher drops produce narrower color stripes. Note that effects like camera flare are not included in the render, and that could result in the appearance difference of the bright light source reflection.*

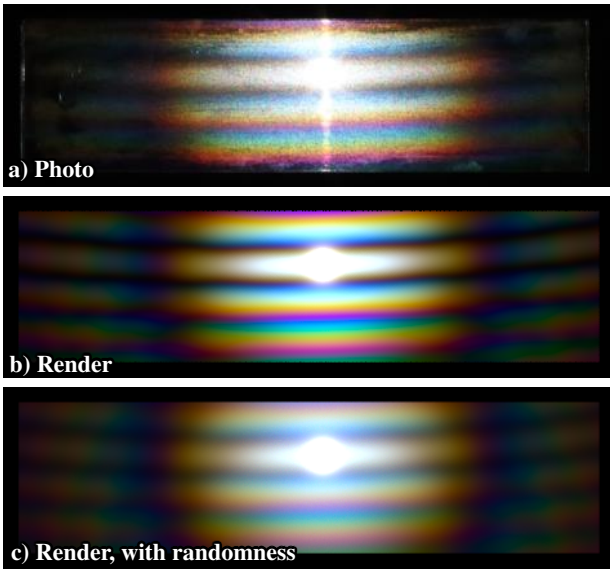

Figure 9: *We validate our Quetelet scattering model using a thin back-surface mirror covered by SiO_2 spheres of uniform size (9.2 μm in diameter). In the photo and the renderings, we can see colorful Mie rings and Quetelet stripes with matching size and orientation, and very similar colors. See Section 4.3 for details.*

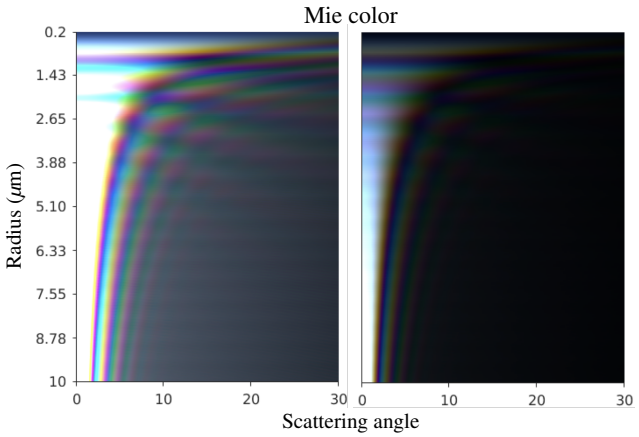

Figure 10: *This figure shows how Mie scattering color varies across wavelengths and scattering angles. The image on the right is a lower-exposure version of the left one to better show the color for small scattering angles (close to forward scattering). This chart illustrates that changes in either particle size or scattering angles give rise to color changes; the larger the particle, the faster the color changes across scattering angles.*

5.1. Steam simulation

For computer graphics, steam is usually modeled in the same way as smoke, as shown in research publications [FSJ01; ZBG15] and visual effects tutorials [Bay19]. Flow simulations are driven by a temperature-dependent buoyancy force. Both temperature and a particle concentration field are advected with the flow, and volumetric scattering is used to render steam as a continuous volume. However, from the captured video, we can tell that steam usually forms in sheet-like patterns and disappears through evaporation rather than only by dissipating into the environment. These characteristics cannot be reproduced very well in traditional smoke simulation. In addition, when looking closely at the steam above a teacup, it is easy to see the discrete water droplets, and their intensity and color depend on their size. Therefore, it is useful to render steam as a discrete medium.

Our goal is to create a visually believable distribution of steam droplets for our rendering system. We achieve this by building on existing fluid simulators used for computer graphics, using a one-way coupling between the fluid simulation and the steam. It is important to note that this is not an accurate physical model for this multi-phase fluid flow, even if the momentum of droplets can be neglected. This is because the simulation does not model the effects of condensation and evaporation on the temperature and pressure of the air. Rather, the simulator is intended to generate visually plausible flows with a reasonable indication of temperature and water content. These can be used with a simple model for droplet formation to generate particle distributions with the right qualitative properties to match the appearance of the real system. In particular, we use the Pyro solver in Houdini 18.5 to simulate the movement of air and water vapor. The simulation outputs velocity, temperature, and concentration fields on voxel grids, which we use to drive the droplet growth computation.

© 2023 Eurographics - The European Association for Computer Graphics and John Wiley & Sons Ltd.

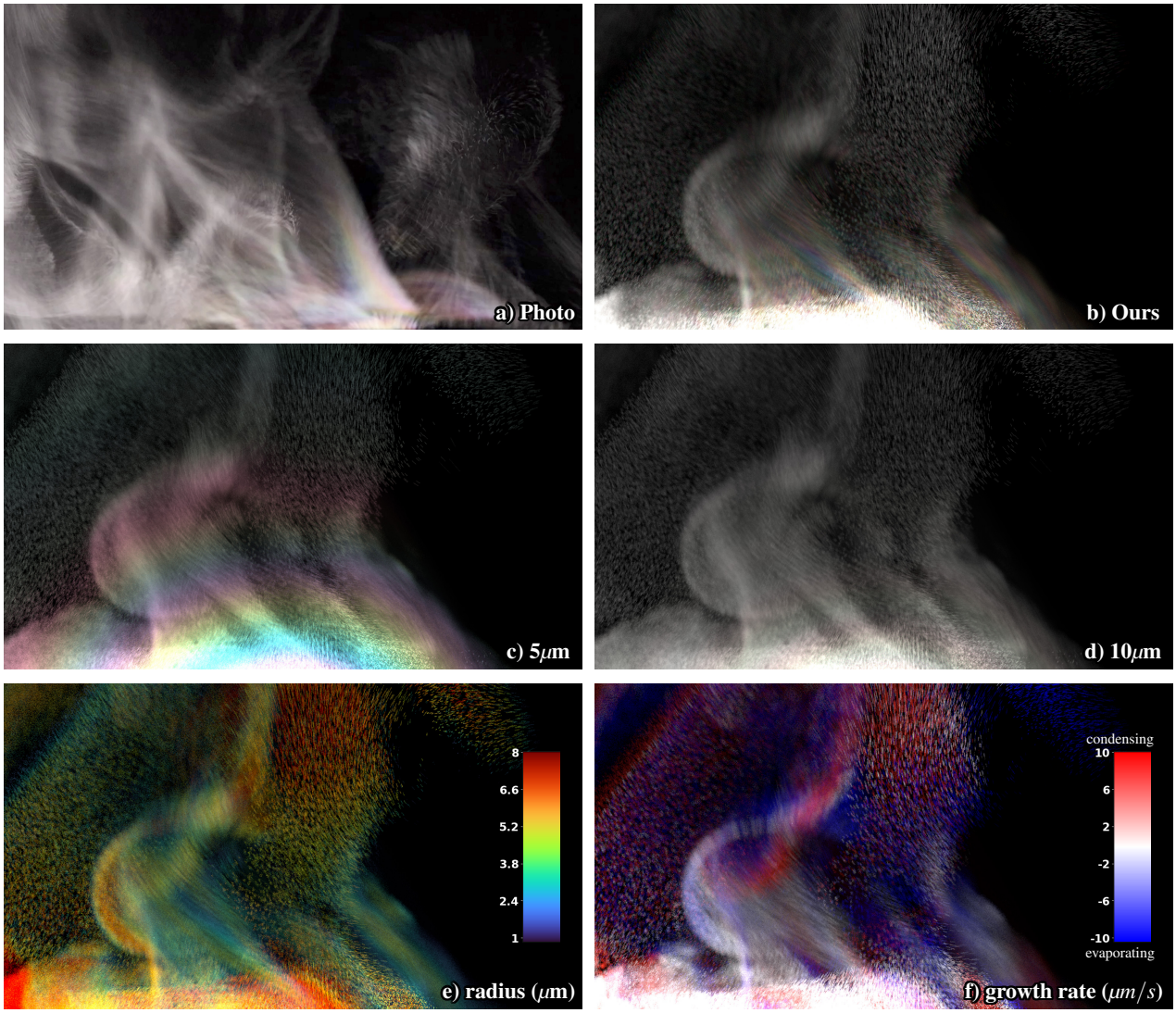

Figure 11: *This figure presents iridescent steam. a) is one frame of our captured steam video. b) is one frame of our steam animation. Similar to the capture, our model is able to reproduce steam that is mostly gray plus some color patterns correlated with the steam flow. We compare to Mie scattering with a uniform particle size in the middle row. In c) and d) all drops are 5μm and 10μm radius respectively. Without size variation we can only produce concentric color arcs around the light source. We refer the reader to our video that shows both the appearance and the dynamics of the steam. The rendered steam in b) is most colorful when the radii e) are small and there is correlation between the size of the drops and the steam flow. In figure f) we color the drops by their growth rate, with a positive value meaning condensing and a negative value corresponding to evaporating. The condensing and evaporating behavior also correlate with the steam flow.*

5.2. Droplet evaporation and condensation

Steam is a multi-phase phenomenon in which water transforms between gaseous and liquid states via evaporation and condensation. Our droplet growth model is based on comparing the current vapor pressure of water to the saturation vapor pressure to determine when condensation and evaporation occur. Saturation vapor pressure is the pressure at which water vapor is in thermodynamic equilibrium with its condensed state. Assuming that the proper condensation nuclei are present, when the local vapor pressure P is higher than saturation pressure, water condenses and droplets grow, and when the pressure is lower, they evaporate and shrink. From the main fluid simulation we can obtain fluid concentration, and we can convert concentration to vapor pressure P by enforcing saturation water pressure at the water surface. We apply the Tetens equation to describe the relationship between saturation vapor pressure and temperature [Leg90].

$$P_s = 0.61078 \exp\left(\frac{17.27T}{T+237.3}\right), \tag{7}$$

© 2023 Eurographics - The European Association
for Computer Graphics and John Wiley & Sons Ltd.

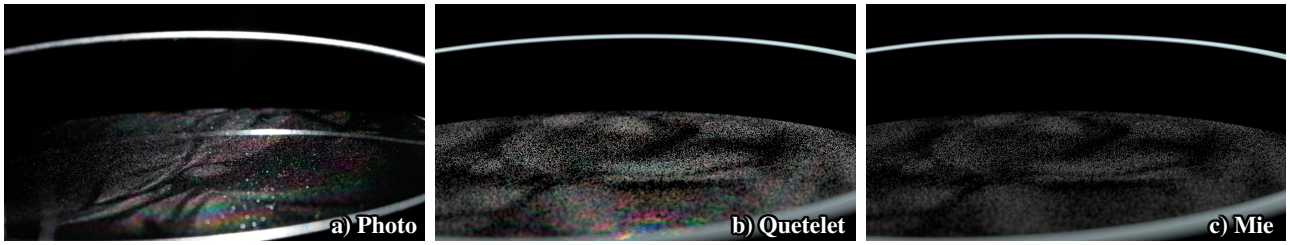

Figure 12: *We render droplets on the water surface using (b) a Quetelet scattering model and (c) Mie scattering. We compare with a photograph (a) and show that the Quetelet scattering model is needed to produce color patterns on the levitating drops. The Mie render is colorless because we are away from the forward scattering direction. Figure 10 shows how Mie color varies with the size of the droplet and the scattering angle. Image (b) is one frame of a Quetelet scattering animation that shows how the color changes over a short period of time. The accompanying video includes a captured video of iridescent levitating drops.*

where temperature T is in degrees Celsius (°C) and saturation vapor pressure P_s is in kilopascals (kPa).

To model the rate of growth as a function of the vapor pressure differential, we turn to a diffusive growth model described by [PK10]. This model considers a radially symmetric diffusion from a motionless drop. As a droplet grows, water vapor flows inward towards the surface while the heat produced by condensation diffuses outward (and vice versa during evaporation). Since irregularities in the flow will balance out rapidly, they assume a steady flow satisfying time-independent diffusion equations. By relating the fluxes of vapor and heat, we arrive at a model for the droplet growth rate:

$$r\frac{dr}{dt} = \frac{D(\rho/\rho_w)(r_s\mathcal{H} - r_s)}{1 + r_s(D/\kappa)\left[L_l^2/\left(C_s R_v T^2\right)\right]} \tag{8}$$

In the above equation, r represents the radius, T represents temperature, and $\mathcal{H}$ represents the ratio between the water vapor pressure (P) and the saturation vapor pressure (P_s). When $\mathcal{H} > 1$, the droplet condenses and grows, and when $\mathcal{H} < 1$, the droplet evaporates and shrinks. ρ represents air density, and ρ_w represents water density. L_l represents the latent heat of condensation, and C_s represents the specific heat of dry air at constant pressure. The saturation mixing ratio $r_s = P_s/(R_v T\rho)$, where R_v is the gas constant for water vapor. D represents the diffusivity of water vapor, which is a function of temperature:

$$D = 2.14 \times 10^{-5}(T/T_f)^{1.94}, \tag{9}$$

where $T_f = 273.15$K and assuming the ambient pressure is one atmosphere. The ratio of the diffusivity of water vapor and heat is approximately $D/\kappa = 1.15$.

Details aside, (8) provides a time derivative of droplet radius that can be computed from the local conditions of temperature and humidity that are output by the simulation.

We simulate droplet evolution as a post-processing step after the main fluid simulation. We first initialize random condensation nuclei uniformly in space with a radius of 0.2μm. At each frame, for each particle, we use the local conditions to compute the right-hand side of (8). Note that in order to account for the conservation of water, we subtract the already condensed water from the available water vapor provided by the main simulation output. We estimate the already condensed water by reading the water content at the current particle and multiplying it by the volume density of condensation nuclei. This assumes that the nearby particles are the same size as the current particle. Then, assuming that the right-hand side of (8) is constant between two frames, we can analytically compute the new radius.

$$r_{n+1} = \sqrt{2(r_n^2/2 + C\Delta t)} \tag{10}$$

where r_n is the radius of the droplet at frame n, C denotes the value of the right-hand side of (8), and Δt is the time between two frames. In our simulation, $\Delta t = 1/60$ s, and the constant right-hand side is a good assumption when the simulation frame rate is 60 fps.

6. Rendering Iridescent Droplets

We implement Mie scattering and Quetelet scattering as two different materials in PBRT-v3 [PJH16] and perform spectral rendering with 50 wavelengths. For shading, we evaluate the Mie scattering and Quetelet scattering distributions on the fly. To render discrete particles, we attach the Mie scattering material and Quetelet scattering material to sphere primitives. We render single scattering only, as the particles are normally well separated, and we use a custom ray tracing primitive for motion blur (Section 6.2).

6.1. Material model implementation

In the material model evaluation, the droplet is considered as a point consistent with the far-field scattering models. In our implementation, light is assumed to be unpolarized on the path tracing level. This assumption is required to integrate with PBRT-v3, which does not model polarization. For our formulation in terms of linearly polarized electric fields, the Jones calculus is simpler and sufficient. The Jones matrices can be converted to Mueller matrices [Sav09] (Appendix C) if the model is to be used in a polarization renderer that works with Stokes vectors. When evaluating the scattering models themselves, we do consider polarization and average the two polarizations to simulate unpolarized light. From the scattering matrix $\mathbf{S}$ we can compute the scattering distribution:

$$f = \frac{1}{k^2 a^2 \pi}\left(|S_{pp}|^2 + |S_{ps}|^2 + |S_{sp}|^2 + |S_{ss}|^2\right) \tag{11}$$

© 2023 Eurographics - The European Association for Computer Graphics and John Wiley & Sons Ltd.

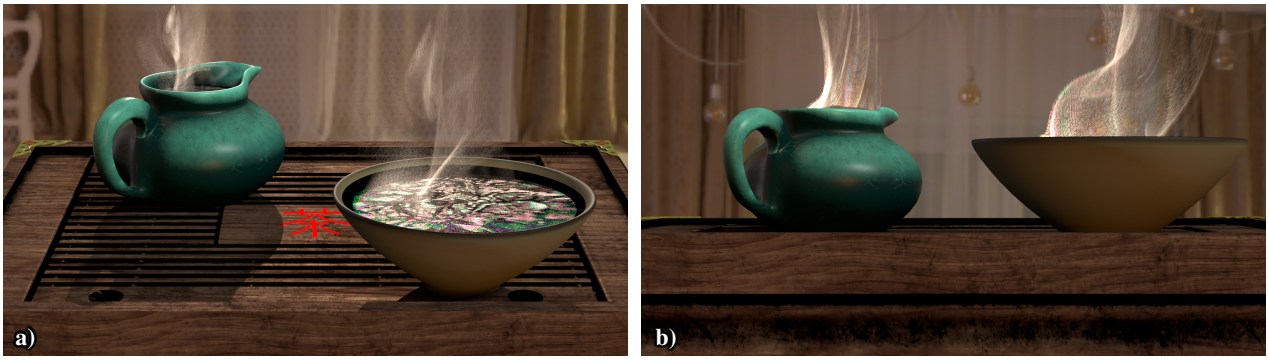

Figure 13: *The figure contains two frames of our animation showcasing iridescent levitating drops (Figure a) and iridescent steam (Figure b). This scene includes an environmental light and a directional light. The animation features changes in lighting and viewing directions. We observe Quetelet scattering patterns on the water surface in the bowl, and the iridescent pattern changes as the angle changes. In the second part of the animation, we see color patterns in the steam that correlate with the steam flow. In Figure b), we see colors in the steam both above the bowl and the pitcher.*

Here k is the wave number and a is the radius used in the scene. In our application, the droplets are always subpixel in size, and we represent them in our scene geometry using individual particles' extinction cross-sections averaged over wavelength. The extinction cross-section of the particles in the wave context is generally larger than the geometric cross-section and is wavelength dependent [vdHul57]. When we evaluate their scattering functions, we normalize based on their extinction cross-section, ensuring energy balance.

We also define a Quetelet BRDF based on the scattering matrix and use it to render surfaces where granularity is not visible. Assuming particles' area density is ρ_a (number of particles per unit area), the Quetelet BRDF is

$$f = \frac{\rho_a}{k^2 a^2 \pi \cos\theta_i} \left(|S_{pp}|^2 + |S_{ps}|^2 + |S_{sp}|^2 + |S_{ss}|^2 \right). \quad (12)$$

For importance sampling the scattering function, we tabulate a Mie scattering table with 50 radius-to-wavelength ratios and 180 scattering angles using an analytic integration method that can integrate Mie scattering over an arbitrary scattering angle range. The Mie scattering table is also used to sample Quetelet scattering.

6.2. Motion blur

It is expensive to render a massive amount of particles with motion blur. The particles can travel far compared to their sizes. As a result, the brute force motion blur, where each ray samples a time and Monte Carlo integration handles time integration, can take a long time to converge because the probability of hitting the particles is low. We accelerate this process by representing the linear trajectory of the particle during the time of one frame as a cylinder with hemispherical end caps and we call it a capsule primitive. We outperform the brute force motion blur by 10x (Figure 14). The probability of hitting the capsule primitive is much higher, leading to faster convergence. This is a technique used in motion blur rendering [NSG11]. Note that since the spheres are very small compared to the distance the ray travels, one needs to be careful with the intersection tests to avoid issues with numerical precision [HGA19].

To properly compute the contribution, we implement a new PBRT integrator that continues a ray after hitting a capsule primitive. It blends the radiance along a ray until it no longer hits a particle (no intersection or intersection with something else). The probability that a ray intersects with the particle given that the ray hits the capsule is computed as the ratio of the particle cross-section over the projected area of the capsule seen by the ray. Algorithm 1 describes the new method. We essentially replace the Monte Carlo time integration with an approximation of the mean value, discarding temporal correlation. A similar approximation is used when computing shadow ray occlusion.

The intersection of the capsule primitive is cheap to compute: We first compute the closest point on the ray to the line connecting the start point and the end point of the particle, which is also the capsule axis. If the closest point lies within the capsule then the intersection is found; If the closest point lies outside the length of the capsule then we compute the distance of the start point and end point of the particle to the ray to check for intersection.

7. Results

In Figure 1, we present a comparison between a real-life capture by Vivien Parmentier and our render of a cup of hot tea. Both images show droplets levitating on the water surface and steam droplets up in the air. Under these specific lighting and viewing conditions, we can observe the Quetelet scattering color on the water surface but no color in the steam. To produce this capture, we use an image texture from another photo to generate droplet density. We predict the height and size of the droplets based on an infrared image we captured. The prediction is done using our empirical model (6). We render the appearance using our Quetelet scattering model and produce an iridescence pattern with similar hues as in the captured image. Note that the water droplets are often well separated from each other, and they can form a granular appearance, not to be confused with Monte Carlo noise, although they may appear similar at times.

In Figure 11, we compare one frame of our capture a) with

© 2023 Eurographics - The European Association
for Computer Graphics and John Wiley & Sons Ltd.

Algorithm 1: Render particles with motion blur with single scattering using capsule primitives.

```
Given ray with start and end;
L ← Spectrum(0); α ← 1; count ← 0;
Russian Roulette termination probability p_RR;
while true do
    t, object = intersect(ray)
    if object is a new particle trace then
        Let p be Pr{ hit particle | hit particle trace }
        Let L_part be the particle's scattered radiance
        L = L + αpL_part
        α = α(1 − p)
    end
    if object is a surface or the background then
        Let L_bg be the reflected or background radiance
        L = L + αL_bg
        break
    end
    ray.start = t + small offset
    count = count + 1
    if count >=10 then
        if random number x < p_RR then
            break
        else
            α = α/(1 − p_RR)
        end
    end
end
return L
```

the renders. To produce image b), we post-process the temperature, concentration, and velocity fields output from an existing fluid simulation. We use our droplet growth model to drive droplet size changes and render the appearance using Mie scattering. Similar to the capture, the render contains colors near the bottom of the frame while the rest of the steam is almost colorless. In images c) and d) we render the steam using Mie scattering with uniform-size spheres. Comparing images a)-d), we observe that size variation is essential to produce steam iridescence that is more similar to the capture, where the color pattern is more correlated with the steam flow. With uniform particle size, we can only produce a fixed concentric arc shape. In Figure e) we color the particles by their sizes and limit the colored range to radius 1-8μm. The steam appearance in b) is most colorful when the radii are small and there is a correlation between the size of the drops and the steam flow. In Figure f) we color the water droplets by their growth rate, with a positive value meaning condensing and a negative value corresponding to evaporating. We limit the colored range to -10 to 10 $\mu m/s$. The condensing and evaporating behavior also correlates with the steam flow. This result demonstrates that size variation is critical to reproduce the distinct color pattern in real steam.

In Figure 12, we show levitating droplets on a water surface using only Mie scattering and a Quetelet scattering model, and compare it to a photograph. Since we are not close enough to the forward scattering direction, Mie scattering produces a colorless appearance. The Quetelet scattering model accounts for interference between different light paths and produces color. The droplet's position, size, and height are predicted using a temperature texture captured by our infrared camera. We also include a short animation showing how the iridescent pattern on the water surface evolves over time.

In Figure 13, we present two frames of an animation that contain both effects. In Figure 13 a), we observe iridescent patterns on the levitating drops above the water surface. In image b), we see colors in the steam both above the bowl and the pitcher. In this scene, there is an environmental light and a directional light. The viewing and lighting directions are opposite and approximately symmetric around the normal of the water surface. In the animation, we start with a fixed camera pose and light direction and show the steam motion. Then, we gradually change the lighting and viewing directions so we shift from view a) to b). In the first part of the animation, we see Quetetlet scattering patterns on the water surface, and they change colors as the angle changes. In the second part of the animation, we see color patterns in the steam that correlate with the steam flow.

We evaluate the performance of rendering sparse particles with motion blur in Figure 14. The acceleration method achieves a 3x and 3.16x reduction in RMSE for an equal time comparison (14 min) with shadowing on and off. When the shadowing is off, the intersected particles are always lit. This corresponds to a 9x and 10x improvement in running time. The three results take 32 spp, 6 spp, and 7 spp, respectively.

Besides the animations of iridescent levitating drops, colorful steam, and the combined scene, we also provide captured videos that record the iridescent appearance along with droplet dynamics.

8. Discussion and Conclusion

In this paper, we reproduce iridescent levitating droplets and colorful steam from a cup of hot tea, and extend the range of particle scattering that one can render. The color patterns on the water surface are a Quetelet scattering phenomenon, where light scattered by the droplets and reflected by the water surface interfere with each other. We examine three different models to perform optical simulation of Quetelet scattering and apply the first-order model that can faithfully produce the effect efficiently. To acquire input for this model, we build a model that relates temperature, droplet height, and size by aligning optical images, infrared images, and renders. To produce colorful steam, we combine size variation with Mie scattering and show that in this way, the steam appearance looks more similar to the captured image than using Mie scattering on uniform-size droplets. We post-process existing steam simulation and combine a diffusion growth model to drive droplet growth. We efficiently render sparse tiny particles with motion blur under a single scattering assumption. Instead of sampling time and using Monte Carlo to handle time integration, we trace particle trajectories and blend the contribution along rays properly, which significantly speeds up the brute force motion blur.

There are some limitations on the simulation side. For levitating droplets, we observe that there is more dynamics in the captured video besides droplet height variation. For example, cracks form on the water surface, and drops disappear individually or as a group.

© 2023 Eurographics - The European Association for Computer Graphics and John Wiley & Sons Ltd.

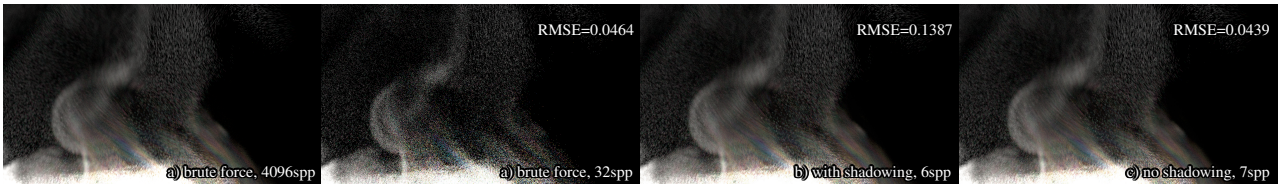

Figure 14: *We compare the performance of the brute force motion blur method with the accelerated method. Although the computation for each ray is more expensive because we need to continue the ray and blend all the contributions along the ray, the overall performance gain is significant. For an equal time comparison, we achieve a 3x and 3.16x reduction in RMSE with shadowing on and off respectively, corresponding to a 9x and 10x speed up in running time.*

To better reproduce this phenomenon, we need to more accurately simulate the convection cells on the water surface and droplet dynamics. For steam drops in the air, the simulation could be improved by accounting for the effects of condensation and evaporation on the temperature and pressure of the air. Also, in future work, the motion of the droplet could be taken into account when simulating droplet growth, and other growth mechanisms such as coalescence might also be relevant.

Our model is not limited to producing a cup of hot tea. We have shown that the Quetelet scattering model can also be applied to render color patterns caused by fine particles on solid surfaces, such as a dusty window or mirror. The model can be extended to handle more diverse effects by using more arbitrarily shaped particles. Our steam model can be adopted to generate color patterns produced by small droplets that undergo phase changes and result in size variation. Examples of such phenomena include sun-lit ice [Gil09] and sun-lit damped wood [Pod07]. Another interesting direction would be to transfer our steam model and develop new volume scattering models for rendering effects such as iridescent cloud, which contains particles with size variation but on a much larger scale.

References

[AK21] AJAEV, V. S. and KABOV, O. A. "Levitation and self-organization of droplets". *Annual Review of Fluid Mechanics* 53 (2021), 203–225 2.

[Bay19] BAY, T. *Pyro I - Smoke & Steam*. 2019. URL: https://www.cgforge.com/course/pyro-i 8.

[BB17] BELCOUR, L. and BARLA, P. "A practical extension to microfacet theory for the modeling of varying iridescence". *ACM Transactions on Graphics (TOG)* 36.4 (2017), 65 2.

[BN08] BRUNETON, E. and NEYRET, F. "Precomputed atmospheric scattering". *Computer graphics forum*. Vol. 27. 4. Wiley Online Library. 2008, 1079–1086 2.

[Boy09] BOYLE, K. *Dusty Window*. 2009. URL: http://www.atoptics.co.uk/fz102.htm 4.

[BV86] BOBBERT, P. and VLIEGER, J. "Light scattering by a sphere on a substrate". *Physica A: Statistical Mechanics and its Applications* 137.1-2 (1986), 209–242 4, 5.

[BVG86] BOBBERT, P., VLIEGER, J., and GREEF, R. "Light reflection from a substrate sparsely seeded with spheres-comparison with an ellipsometric experiment". *Physica A: Statistical Mechanics and its Applications* 137.1-2 (1986), 243–257 2, 4, 5.

[DWMG16] DONG, Z., WALTER, B., MARSCHNER, S., and GREENBERG, D. P. "Predicting Appearance from Measured Microgeometry of Metal Surfaces". *ACM Trans. Graph.* 35.1 (Dec. 2016). ISSN: 0730-0301. DOI: 10.1145/2815618. URL: https://doi.org/10.1145/2815618 3.

[FCJ07] FRISVAD, J. R., CHRISTENSEN, N. J., and JENSEN, H. W. "Computing the scattering properties of participating media using Lorenz-Mie theory". *ACM SIGGRAPH 2007 papers*. 2007, 60–es 2.

[FDN17] FEDORETS, A., DOMBROVSKY, L., and NOSONOVSKY, M. "Comment on Levitation and Self-Organization of Liquid Microdroplets over Dry Heated Substrates". *arXiv preprint arXiv:1711.02709* (2017) 2.

[Fed04] FEDORETS, A. A. "Droplet cluster". *Journal of Experimental and Theoretical Physics Letters* 79.8 (2004), 372–374 2, 7.

[Fed05] FEDORETS, A. A. "On the mechanism of noncoalescence in a droplet cluster". *Journal of Experimental and Theoretical Physics Letters* 81.9 (2005), 437–441 2, 7.

[Fed12] FEDORETS, A. "Mechanism of stabilization of location of a droplet cluster above the liquid-gas interface". *Technical Physics Letters* 38.11 (2012), 988–990 2.

[FSJ01] FEDKIW, R., STAM, J., and JENSEN, H. W. "Visual simulation of smoke". *Proceedings of the 28th annual conference on Computer graphics and interactive techniques*. 2001, 15–22 3, 8.

[Ger97] GERMER, T. A. "Angular dependence and polarization of out-of-plane optical scattering from particulate contamination, subsurface defects, and surface microroughness". *Applied Optics* 36.33 (1997), 8798–8805 2, 5.

[GHC*22] GUO, J., HU, B., CHEN, Y., LI, Y., GUO, Y., and YAN, L.-Q. "Rendering discrete participating media using geometrical optics approximation". *Computational Visual Media* 8.3 (2022), 425–444 3.

[Gil09] GILDER, D. *Sun-warmed Ice*. 2009. URL: http://www.atoptics.co.uk/fz163.htm 13.

[GJZ21] GUO, Y., JARABO, A., and ZHAO, S. "Beyond mie theory: systematic computation of bulk scattering parameters based on microphysical wave optics". *ACM Transactions on Graphics (TOG)* 40.6 (2021), 1–12 2.

[GMG*20] GUILLÉN, I., MARCO, J., GUTIERREZ, D., JAKOB, W., and JARABO, A. "A general framework for pearlescent materials". *ACM Transactions on Graphics (TOG)* 39.6 (2020), 1–15 3.

[GRBN07] GU, J., RAMAMOORTHI, R., BELHUMEUR, P. N., and NAYAR, S. K. "Dirty Glass: Rendering Contamination on Transparent Surfaces." *Rendering Techniques*. 2007, 159–170 2.

[HGA19] HAINES, E., GÜNTHER, J., and AKENINE-MÖLLER, T. "Precision Improvements for Ray/Sphere Intersection". *Ray Tracing Gems*. Springer, 2019, 87–94 11.

[HP17] HOLZSCHUCH, N. and PACANOWSKI, R. "A two-scale microfacet reflectance model combining reflection and diffraction". *ACM Transactions on Graphics (TOG)* 36.4 (2017), 1–12 3.

© 2023 Eurographics - The European Association
for Computer Graphics and John Wiley & Sons Ltd.

[HTSG91] He, X. D., Torrance, K. E., Sillion, F. X., and Greenberg, D. P. "A comprehensive physical model for light reflection". *ACM SIGGRAPH computer graphics*. Vol. 25. 4. ACM. 1991, 175–186 3.

[HW12] Hosek, L. and Wilkie, A. "An analytic model for full spectral sky-dome radiance". *ACM Transactions on Graphics (TOG)* 31.4 (2012), 1–9 2.

[Leg90] Legg, B. "Principles of Environmental Physics . By JL Monteith and MH Unsworth. Sevenoaks, Kent: Edward Arnold (1990), pp. 291,£ 14.95, hardback£ 30.00." *Experimental Agriculture* 26.4 (1990), 447–447 9.

[Lei95] Leipelt, A. "Ray tracing a swept sphere". *Graphics Gems V*. Elsevier, 1995, 258–267 3.

[Mac08] Mackowski, D. W. "Exact solution for the scattering and absorption properties of sphere clusters on a plane surface". *Journal of Quantitative Spectroscopy and Radiative Transfer* 109.5 (2008), 770–788 2.

[MPG*16] Müller, T., Papas, M., Gross, M., Jarosz, W., and Novák, J. "Efficient rendering of heterogeneous polydisperse granular media". *ACM Transactions on Graphics (TOG)* 35.6 (2016), 1–14 3.

[MWM07] Moon, J. T., Walter, B., and Marschner, S. R. "Rendering discrete random media using precomputed scattering solutions". *Proceedings of the 18th Eurographics conference on Rendering Techniques*. 2007, 231–242 3.

[NSG11] Navarro, F., Serón, F. J., and Gutierrez, D. "Motion blur rendering: State of the art". *Computer Graphics Forum*. Vol. 30. 1. Wiley Online Library. 2011, 3–26 2, 3, 11.

[NSTN93] Nishita, T., Sirai, T., Tadamura, K., and Nakamae, E. "Display of the earth taking into account atmospheric scattering". *Proceedings of the 20th annual conference on Computer graphics and interactive techniques*. 1993, 175–182 2.

[PJH16] Pharr, M., Jakob, W., and Humphreys, G. *Physically based rendering: From theory to implementation*. Morgan Kaufmann, 2016 10.

[PK10] Pruppacher, H. and Klett, J. "Diffusion growth and evaporation of water drops and snow crystals". *Microphysics of Clouds and Precipitation*. Springer, 2010, 502–567 10.

[PK12] Pruppacher, H. R. and Klett, J. D. *Microphysics of Clouds and Precipitation: Reprinted 1980*. Springer Science & Business Media, 2012 3.

[Pod07] Podravec, D. *Damp Wood*. 2007. URL: http://www.atoptics.co.uk/droplets/iridim32.htm 13.

[Sav09] Savenkov, S. N. "Jones and Mueller matrices: structure, symmetry relations and information content". *Light Scattering Reviews 4*. Springer, 2009, 71–119 10.

[SML*12] Sadeghi, I., Munoz, A., Laven, P., Jarosz, W., Seron, F., Gutierrez, D., and Jensen, H. W. "Physically-based simulation of rainbows". *ACM Transactions on Graphics (TOG)* 31.1 (2012), 1–12 2, 7.

[SS09] Suhr, W. and Schlichting, H. J. "Quételet's fringes due to scattering by small spheres just above a reflecting surface". *Applied optics* 48.26 (2009), 4978–4984 2, 6.

[SSY22] Steinberg, S., Sen, P., and Yan, L.-Q. "Towards practical physical-optics rendering". *ACM Transactions on Graphics (TOG)* 41.4 (2022), 1–24 3.

[Sta99a] Stam, J. "Diffraction shaders". *Siggraph*. Vol. 99. 1999, 101–110 3.

[Sta99b] Stam, J. "Stable fluids". *Proceedings of the 26th annual conference on Computer graphics and interactive techniques*. 1999, 121–128 3.

[Ste09] Stepanenko, S. *Teacup Vapor*. 2009. URL: http://www.atoptics.co.uk/fz210.htm 3.

[SY21] Steinberg, S. and Yan, L.-Q. "A generic framework for physical light transport". *ACM Transactions on Graphics (TOG)* 40.4 (2021), 1–20 3.

[SYK*17] Shkurko, K., Yuksel, C., Kopta, D., Mallett, I., and Brunvand, E. "Time interval ray tracing for motion blur". *IEEE transactions on visualization and computer graphics* 24.12 (2017), 3225–3238 3.

[THDD20] Tessari, L., Hanika, J., Dachsbacher, C., and Droske, M. "Temporal Normal Distribution Functions." *EGSR (DL)*. 2020, 1–12 3.

[UONI15] Umeki, T., Ohata, M., Nakanishi, H., and Ichikawa, M. "Dynamics of microdroplets over the surface of hot water". *Scientific reports* 5 (2015), 8046 2, 7.

[Van85] Van Wijk, J. J. "Ray tracing objects defined by sweeping a sphere". *Computers & Graphics* 9.3 (1985), 283–290 3.

[vdHul57] Van de Hulst, H. C. *Light scattering by small particles*. John Wiley & Sons, 1957 2, 6, 11.

[WD98] Wriedt, T. and Doicu, A. "Light scattering from a particle on or near a surface". *Optics communications* 152.4-6 (1998), 376–384 2.

[Wen07] Wenzel, C. "Real-Time atmospheric effects in games revisited". *Game Developers Conference*. 2007, 551–556 2.

[WVJH17] Werner, S., Velinov, Z., Jakob, W., and Hullin, M. B. "Scratch iridescence: Wave-optical rendering of diffractive surface structure". *ACM Transactions on Graphics (TOG)* 36.6 (2017), 1–14 3.

[XWM*20] Xia, M., Walter, B., Michielssen, E., Bindel, D., and Marschner, S. "A wave optics based fiber scattering model". *ACM Transactions on Graphics (TOG)* 39.6 (2020), 1–16 3.

[YHW*18] Yan, L.-Q., Hašan, M., Walter, B., Marschner, S., and Ramamoorthi, R. "Rendering Specular Microgeometry with Wave Optics". *ACM Trans. Graph.* 37.4 (July 2018), 75:1–75:10. ISSN: 0730-0301. DOI: 10.1145/3197517.3201351. URL: http://doi.acm.org/10.1145/3197517.3201351 3.

[ZBG15] Zhang, X., Bridson, R., and Greif, C. "Restoring the missing vorticity in advection-projection fluid solvers". *ACM Transactions on Graphics (TOG)* 34.4 (2015), 1–8 3, 8.

[ZKAK17] Zaitsev, D. V., Kirichenko, D. P., Ajaev, V. S., and Kabov, O. A. "Levitation and self-organization of liquid microdroplets over dry heated substrates". *Physical review letters* 119.9 (2017), 094503 2.

[ZZ20] Zhang, C. and Zhao, S. "Multi-Scale Appearance Modeling of Granular Materials with Continuously Varying Grain Properties". (2020) 3.

Appendix A: Fresnel reflection and transmission matrices

The reflection and transmission matrices are

$$\mathbf{F} = \begin{pmatrix} r_p & 0 \\ 0 & r_s \end{pmatrix}, \mathbf{T} = \begin{pmatrix} t_p & 0 \\ 0 & t_s \end{pmatrix}. \tag{13}$$

where r_p, r_s, t_p, t_s are the complex amplitude reflection and transmission coefficients for parallel (p) and perpendicular (s) polarization.

$$\begin{aligned} r_p &= \frac{n_2 \cos\theta_\mathrm{i} - n_1 \cos\theta_\mathrm{t}}{n_2 \cos\theta_\mathrm{i} + n_1 \cos\theta_\mathrm{t}} \\ r_s &= \frac{n_1 \cos\theta_\mathrm{i} - n_2 \cos\theta_\mathrm{t}}{n_1 \cos\theta_\mathrm{i} + n_2 \cos\theta_\mathrm{t}} \\ t_p &= \frac{2 n_1 \cos\theta_\mathrm{i}}{n_2 \cos\theta_\mathrm{i} + n_1 \cos\theta_\mathrm{t}} \\ t_s &= \frac{2 n_1 \cos\theta_\mathrm{i}}{n_1 \cos\theta_\mathrm{i} + n_2 \cos\theta_\mathrm{t}} \end{aligned} \tag{14}$$

© 2023 Eurographics - The European Association for Computer Graphics and John Wiley & Sons Ltd.

In the above equations n_1 and n_2 are refractive indices of the two media; θ_i and θ_t are the incident and transmitted angles.

Appendix B: Quetelet scattering on two specular surfaces

We can generalize Quetetlet scattering to more than one specular surface beneath a sphere. For the validation test (Figure 9), we have two specular surfaces beneath a sphere. In addition to the four components used in the one specular surface case (Equation 5), another two components contribute significantly:

$$\begin{aligned} \mathbf{S_V} &= \alpha_2 \mathbf{R_{II}^{out}} \mathbf{S_{Mie}} \mathbf{R_{II}^{in}} \mathbf{T_{i21}} \mathbf{F_{i2}} \mathbf{T_{i12}}, \\ \mathbf{S_{VI}} &= \beta_2 \mathbf{T_{s21}} \mathbf{F_{s2}} \mathbf{T_{s12}} \mathbf{R_{III}^{out}} \mathbf{S_{Mie}} \mathbf{R_{III}^{in}}. \end{aligned} \tag{15}$$

where $\alpha_2 = e^{2j\eta kh\cos\theta_{it}}$ and $\beta_2 = e^{2j\eta kh\cos\theta_{st}}$ are the phase associated with the path-length difference between the first and the second specular surface; η is the index of refraction of the material (glass in the validation) and h_2 is the height between the two surfaces. **F**'s are diagonal matrices where the diagonal entries are complex amplitude reflection coefficients corresponding to the bottom surface. **T**'s are diagonal matrices where the diagonal entries are complex amplitude transmission coefficients corresponding to the first surface. The calculation of **F** and **T** matrices is specified in Appendix A. **R** and $\mathbf{S_{Mie}}$ are the same as they are in Equation 5.

Appendix C: Mueller and Jones matrix

A Jones matrix **J** can be transformed into the corresponding Mueller matrix **M** via

$$\mathbf{M} = \mathbf{A}(\mathbf{J} \otimes \mathbf{J}^*)\mathbf{A}^{-1} \tag{16}$$

where $\otimes$ denotes the tensor product and

$$\mathbf{A} = \begin{pmatrix} 1 & 0 & 0 & 1 \\ 1 & 0 & 0 & -1 \\ 0 & 1 & 1 & 0 \\ 0 & i & -i & 0 \end{pmatrix}. \tag{17}$$

© 2023 Eurographics - The European Association
for Computer Graphics and John Wiley & Sons Ltd.